Transition between amplified spontaneous emission and superfluorescence in a longitudinally pumped medium by an x-ray free-electron-laser pulse

Yu-Hung Kuan and Wen-Te Liao*
Department of Physics, National Central University, Taoyuan City 32001, Taiwan

(Received 21 November 2018; accepted 17 January 2020; published 24 February 2020)

The transition from the amplification of spontaneous emission to superfluorescence in a three-level and swept-gain medium excited by an x-ray free-electron-laser pulse is theoretically investigated. Given the specific timescale of an x-ray free-electron-laser pulse, we investigate the swept pumping process in detail, and our results show that the temporal structure of an x-ray free-electron-laser pulse plays a more critical role than its peak intensity does for producing population inversion. The typical watershed of two radiant regions depends on the optical depth of the gain medium for a given coherence time, namely, the particle number density and medium length are equally important. However, we find that medium length plays a more important role than particle density for making the forward-backward asymmetry. The transient gain length and the total medium length are identified as two important factors to observe length-induced backward transition. The present results suggest an application of parametric controls over a single-pass-amplified light source.

DOI: 10.1103/PhysRevA.101.023836

I. INTRODUCTION

Absorption, stimulated emission, and spontaneous emission of photons are three fundamental processes of light-matter interaction. However, a collection of excited atoms emits light differently from what a single atom does. One type of such collective light emission was first theoretically studied in Dicke's pioneering and seminal work of superfluorescence (SF) [1]. While in free space a wave packet of photons isotropically emitted by a single atom behaves like it is exponentially decaying with a duration of an excited-state lifetime, SF from multiple atoms with particle density n for a given sample length L acts as a directional light burst characterized by its peak intensity, duration, and time delay, which are proportional to n^2, n^{-1}, and n^{-1}, respectively [2,3]. SF was first experimentally realized in room-temperature HF gas [4] and subsequently observed in, e.g., sodium [5], cesium [6], rubidium atoms [7], solid-state $KCl : O_2^-$ [8,9], and in plasma [10,11]. More recently, the development of a free electron laser (FEL) [12] has lead to further advancements, such as the observation of EUV-FEL-induced SF in helium gas [13], XUV-FEL-induced SF in xenon gas [14], and FEL superfluorescence [15]. Apart from typical three-level Λ-type atomic systems [6,13,16–18], a V-type system [19,20] has also been theoretically investigated.

Another kind of collective emission is the so-called amplification of spontaneous emission (ASE) [3,21–24], namely, radiation due to spontaneous emission from a single emitter is amplified when it propagates through an excited sample. While ASE is also directional due to the geometry of the inverted medium, the time structure of ASE is quite distinct from that of SF, e.g., the peak intensity does not behave as n^2 [9,25]. Utilizing the ASE mechanism, an atomic inner shell laser pumped by an x-ray free electron laser (XFEL) has recently been achieved [22–24]. While this achievement [22,24] has become a milestone within the field of x-ray quantum optics [26–38], XFEL-induced SF has never been studied. Moreover, SF and ASE are independently investigated in most works with only a few examples touching on both [9,39–43]. Studying XFEL-pumped SF, as well as the transition from ASE to SF using XFEL, is therefore interesting and timely.

Most theoretical studies of ASE or SF rely on three assumptions: (i) a completely inverted medium as the initial condition [3,25,44,45], (ii) a swept-gain amplifier excited by an oversimplified δ-function pulse [46–48], and (iii) only forward emission of light [23,25,43–47]. In view that XFEL pulse duration may be greater than the excited-state lifetime [22,24], the assumption (ii) [46–48] is unrealistic. One therefore has to carefully deal with the pumping process. We use (a) a swept-gain amplifier excited by a short XFEL pumping pulse with a duration of a few tens femtoseconds [49] and (b) a set of equations describing both the forward and backward emission. Our detailed study of this issue identifies the mechanism breaking the forward and backward symmetry and demonstrates that the time structure of the pumping pulse is highly critical for producing population inversion. Typically, the ASE-SF transition depends only on $\tau_2 \gg \sqrt{\tau_R \tau_D}$ or $\tau_R \ll \tau_2 \ll \sqrt{\tau_R \tau_D}$, where τ_2 is the coherence time of the transition, τ_R the characteristic duration of SF, and τ_D the SF delay time [9,25,50]. The definition of τ_R and τ_D shows that the length of a medium and particle density are equally important for ASE-SF transition. However, our study on the pumping process shows that the choice of medium length plays a more important role than particle density does for observing backward emission, namely, medium-length-induced ASE-SF transition can happen to the backward emission. Apart from the typical averaged temporal behavior of emitted light pulses,

*wente.liao@g.ncu.edu.tw

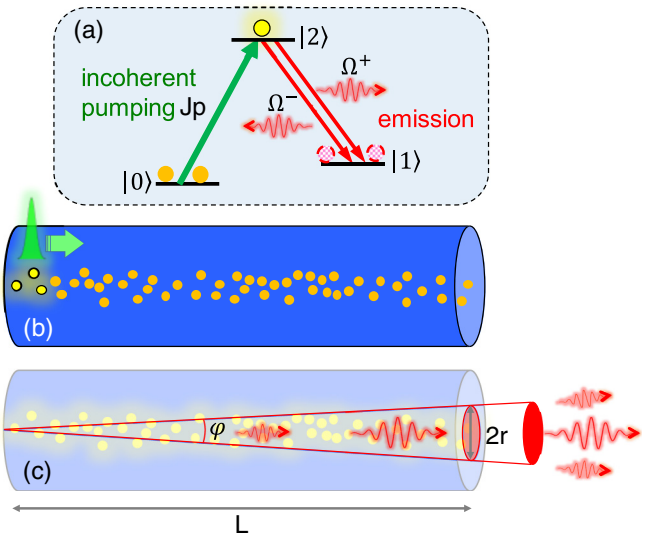

FIG. 1. (a) Three-level Λ-type scheme. Transition $|0\rangle \rightarrow |2\rangle$ is incoherently pumped by a short pumping laser pulse J_p (green upward arrow). Atoms promoted to state $|2\rangle$ subsequently decay and become state $|1\rangle$. Atoms that undergo the transition $|2\rangle \rightarrow |1\rangle$ emit photons (red downward arrows) in the forward and backward direction with equal probability. (b) Atoms in state $|0\rangle$ (orange dots) are initially prepared in a gas cell. When a pumping pulse (green filled Gaussian pulse) is traveling through, atoms are promoted to state $|2\rangle$ (yellow filled circles) in a region defined by the spot size and path of the pumping pulse J_p. (c) φ in Eq. (16) represents the solid angle within which the emitted photons due to transition $|2\rangle \rightarrow |1\rangle$ get amplified in the forward direction. φ is determined by the length L and the transverse radius r of the medium.

we show that both the averaged spectrum and the histogram of emitted photon number manifest the ASE-SF transition. Our results therefore give useful hints for quantifying the XFEL-pumped light source and demonstrate in what parameter region the transition may occur. The present results suggest an application of modifying the properties of a single-pass light source [22–24,51–53] via the transition between ASE and SF induced by the change of optical depth of the gain medium or by the variety of a pumping pulse.

This paper is organized as follows. In Sec. II, we describe our system and theoretical model using the Maxwell-Bloch equation. In Sec. III, we present our analysis of the production of population inversion. In Sec. IV, we numerically solve these coupled equations and discuss the transition between ASE and SF. In Sec. V, the length effects for forward-backward asymmetry are discussed. In Sec. VI, we demonstrate the transition between ASE and SF induced by the variety of pumping laser parameters. A summary is present in Sec. VII.

II. MODEL

Figure 1(a) illustrates our three-level Λ-type system. A pumping light pulse of intensity J_p incoherently drives transition $|0\rangle \rightarrow |2\rangle$, e.g., ionization, when propagating through a one-dimensional gas medium as demonstrated in Fig. 1(b). The orange dots and yellow filled circles, respectively, denote particles in states $|0\rangle$ and $|2\rangle$. For simplicity, promoted particles in state $|2\rangle$ subsequently experience only one decay channel $|2\rangle \rightarrow |1\rangle$ and emit photons in both the forward and backward direction with equal probability (red wiggled arrows). Red dashed and filled circles represent decayed particles in state $|1\rangle$, and the green Gaussian pulse depicts J_p. We numerically analyze the emission behavior for different parameters of the medium and that of J_p. The Maxwell-Bloch equation [2,23,25,46,54,55] with forward-backward decomposition [34,56,57] is used to describe the dynamics, including the incoherent and longitudinal pumping:

$$\partial_t \rho_{00} = -\sigma J_p \rho_{00}, \tag{1}$$

$$\partial_t \rho_{11} = \Gamma \rho_{22} - \frac{i}{2}\left(\Omega^+ \rho_{21}^{+*} - \Omega^{+*} \rho_{21}^{+}\right) - \frac{i}{2}\left(\Omega^- \rho_{21}^{-*} - \Omega^{-*} \rho_{21}^{-}\right), \tag{2}$$

$$\partial_t \rho_{22} = \sigma J_p \rho_{00} - \Gamma \rho_{22} + \frac{i}{2}\left(\Omega^+ \rho_{21}^{+*} - \Omega^{+*} \rho_{21}^{+}\right) + \frac{i}{2}\left(\Omega^- \rho_{21}^{-*} - \Omega^{-*} \rho_{21}^{-}\right), \tag{3}$$

$$\partial_t \rho_{21}^{+} = -\frac{\Gamma}{2}\rho_{21}^{+} - \frac{i}{2}(\rho_{22} - \rho_{11})\Omega^{+} + F^{+}, \tag{4}$$

$$\partial_t \rho_{21}^{-} = -\frac{\Gamma}{2}\rho_{21}^{-} - \frac{i}{2}(\rho_{22} - \rho_{11})\Omega^{-} + F^{-}, \tag{5}$$

$$\frac{1}{c}\partial_t J_p + \partial_z J_p = -n\rho_{00}\sigma J_p, \tag{6}$$

$$\frac{1}{c}\partial_t \Omega^{+} + \partial_z \Omega^{+} = i\eta \rho_{21}^{+}, \tag{7}$$

$$\frac{1}{c}\partial_t \Omega^{-} - \partial_z \Omega^{-} = i\eta \rho_{21}^{-}. \tag{8}$$

Here $\rho_{ii} = B_i B_i^*$ is the diagonal density matrix element, and $\rho_{21}^{+(-)}$ is the forward (backward) component of the coherence $B_2 B_1^*$ for state vector $\sum_{i=0}^{2} B_i |i\rangle$. $\Gamma = 1/\tau_2$ denotes the spontaneous decay rate of state $|2\rangle$, τ_2 the lifetime of state $|2\rangle$, and σ the absorption cross section of transition $|0\rangle \rightarrow |2\rangle$. $\Omega^{+(-)}$ denotes the slowly varying Rabi frequency of forward (backward) emission from the $|2\rangle \rightarrow |1\rangle$ transition. c is the speed of light in vacuum, n the number density of particles, and $\eta = \Gamma\alpha/(2L)$ the light-matter coupling constant. $\alpha = n\sigma_r L$ is the optical depth of the $|1\rangle \rightarrow |2\rangle$ transition. L is the length of the medium, $\sigma_r = 3\lambda^2/(2\pi)$ the resonant cross section of transition $|1\rangle \rightarrow |2\rangle$, and λ the wavelength of the $|1\rangle \rightarrow |2\rangle$ transition. Together with initial and boundary conditions,

$$\rho_{ij}(0, z) = \delta_{i0}\delta_{j0}, \tag{9}$$

$$\rho_{21}^{\pm}(0, z) = 0, \tag{10}$$

$$J_p(0, z) = 0, \tag{11}$$

$$\Omega^{\pm}(0, z) = 0, \tag{12}$$

$$J_p(t, 0) = \frac{n_p}{\pi^{3/2} r^2 \tau_p} \exp\left[-\left(\frac{t - \tau_i}{\tau_p}\right)^2\right], \tag{13}$$

$$\Omega^{+}(t, 0) = 0, \tag{14}$$

$$\Omega^{-}(t, L) = 0, \tag{15}$$

TABLE I. Quantities used in each figure. The common quantities are $c = 3 \times 10^8$ m/s, vacuum permittivity $\varepsilon_0 = 8.85 \times 10^{-12}$ F/m, $\sigma = 3.336 \times 10^{-23}$ m^2, $\sigma_r = 6.4 \times 10^{-18}$ m^2, $\omega = 1.29 \times 10^6$ rad THz, $\lambda = 1.46$ nm, and $d = 3.33 \times 10^{-31}$ C m. The symbol V stands for variable.

Notation	Fig. 2(a)	Fig. 2(b)	Fig. 3	Figs. 4, 9 & 7	Figs. 5 & 8	Fig. 6	Fig. 10
φ (μrad)	12.56	12.56	12.56	V	V	V	12.56
τ_2 (ps)	1	100	0.01	1	100	0.01	1
Γ (THz)	1	0.01	100	1	0.01	100	1
n (cm^{-3})	3×10^{16}	3×10^{16}	3×10^{16}	V	V	V	5×10^{17}
L (mm)	1	1	1	V	V	V	0.16
α	192	192	192	V	V	V	512
η (THz/mm)	96	0.96	9600	V	V	V	1600
τ_p (fs)	60	60	V	60	60	60	60
r (μm)	2	2	2	2	2	2	V
τ_i (ps)	0.3	30	0.3	0.24	0.24	0.24	0.24
n_p	30×10^{12}	30×10^{12}	V	30×10^{12}	30×10^{12}	30×10^{12}	V

where δ_{ij} is Kronecker delta symbol, and r denotes the radius of the J_p laser spot which determines the transverse radius of the gain medium. n_p, τ_p, and τ_i are the number of photons, the pulse duration, and the peak instant of the incident pumping laser pulse, respectively. The forward (backward) emission process starts from Gaussian white noise $F^{+(-)}$ obeying the δ correlation function [2,3,23,44,45],

$$\langle F^{\pm}(\tau)F^{\pm *}(t)\rangle = \frac{\varphi\rho_{22}\Gamma^2\omega^2}{48n\pi^2c^3}\delta(\tau - t), \tag{16}$$

where ω is the angular frequency of the $|1\rangle \rightarrow |2\rangle$ transition, $\delta(\tau - t)$ the Dirac delta function, and

$$\varphi = \int_0^{2\pi} d\phi \int_0^{\tan^{-1}\left(\frac{r}{L}\right)} \sin\theta d\theta = 2\pi - \frac{2\pi}{\sqrt{1 + \frac{r^2}{L^2}}}$$

the solid angle for collecting emitted photons in the forward and backward direction. Based on an experimental facts [58] and [3], we use

$$\langle F^{\pm}(\tau)F^{\mp *}(t)\rangle = 0.$$

The quantity of all notations used for each figure in what follows is listed in Table I. Figure 1(c) illustrates the solid angle φ used in Eq. (16) [46]. φ is determined by the geometry of the gain medium, i.e., an ensemble of atoms longitudinally pumped to state $|2\rangle$ by a J_p pulse. φ is therefore affected by the length of the medium L and the radius r of the J_p laser spot. Those photons randomly emitted within φ will interact with most of the excited atoms and lead to, e.g., stimulated emission. The value from the complete form of φ is used in all of our numerical calculations, and φ can be simplified to an intuitive value $\pi r^2/L^2$ for typical theoretical studies since $r \ll L$ is implicitly assumed in the one-dimensional model. However, in realistic systems, diffraction (three-dimensional effects) can limit the effective solid angle to λ^2/r^2 and can change the simulation results. This problem is associated with Fresnel number **F** [3] and will be discussed in Sec. IV. The ensemble average of temporal intensity $\langle I^{\pm}(t)\rangle$ is defined as

$$\langle I^{+}(t)\rangle = \frac{1}{N_e}\sum_{n=1}^{N_e}|\Omega_n^{+}(t, L)|^2,$$
$$\langle I^{-}(t)\rangle = \frac{1}{N_e}\sum_{n=1}^{N_e}|\Omega_n^{-}(t, 0)|^2, \tag{17}$$

and the ensemble average of spectral intensity $\langle S^{\pm}(\omega)\rangle$ is defined as

$$\langle S^{+}(\omega)\rangle = \frac{1}{N_e}\sum_{n=1}^{N_e}\left|\int_{-\infty}^{\infty}\Omega_n^{+}(t, L)e^{i\omega t}dt\right|^2,$$
$$\langle S^{-}(\omega)\rangle = \frac{1}{N_e}\sum_{n=1}^{N_e}\left|\int_{-\infty}^{\infty}\Omega_n^{-}(t, 0)e^{i\omega t}dt\right|^2. \tag{18}$$

Here $\Omega_n^{\pm}$ is the output $\Omega^{\pm}$ of the nth simulation, and $N_e = 1000$ is the sample size. Our sample size of 1000 is chosen by a series of numerical tests showing that convergence occurs in a range of $N_e = 500$–900, depending on parameters.

III. ANALYTICAL SOLUTIONS

Given the XFEL pulse duration $\leqslant$100 fs and the possible wide range of τ_2 for different systems, it is necessary to analyze the influence of the temporal structure of the pumping pulse on the production of population inversion. In this section we analyze the pumping process in the region of $|\Omega^{\pm}| \ll \Gamma < J_p\sigma$, namely, the pumping rate is greater than the excited-state decay rate and photon emission rate, which allows for the production of population inversion. By first using $\rho_{00}(t, z) = 1$, the solution of Eq. (6) reads

$$J_p(t, z) = \frac{n_p}{\pi^{3/2}r^2\tau_p}\exp\left[-n\sigma z - \left(\frac{t - \tau_i - \frac{z}{c}}{\tau_p}\right)^2\right]. \tag{19}$$

In the parameter region of Figs. 2 and 3, $\exp(-n\sigma L) > 0.98$, one can therefore neglect the attenuation of J_p for both cases. The solution of Eq. (1) is then given by

$$\rho_{00}(t, z) \approx \exp\left\{-\frac{n_p\sigma}{2\pi r^2}\left[1 + \mathrm{erf}\left(\frac{t - \tau_i - \frac{z}{c}}{\tau_p}\right)\right]\right\}. \tag{20}$$

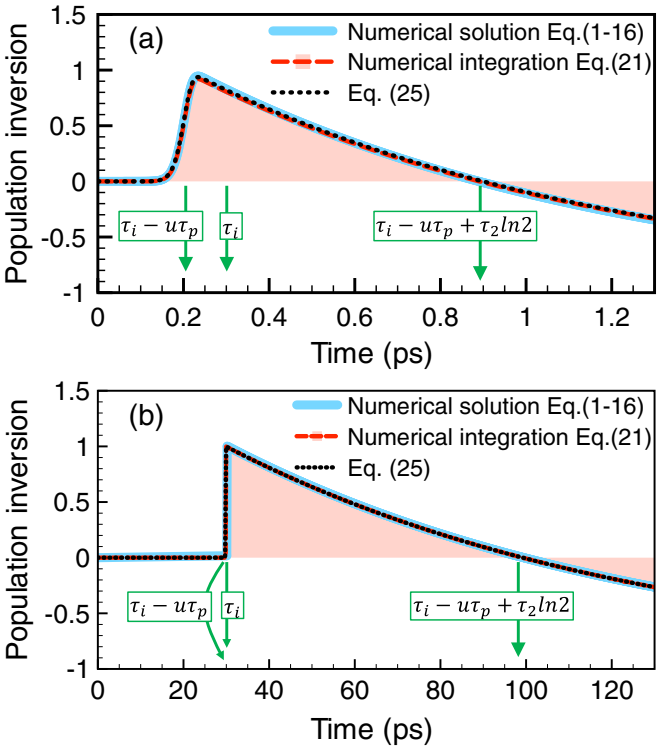

FIG. 2. Population inversion $I(t, z = 0)$ for (a) $(\tau_2, \tau_i) = (1\ \text{ps}, 0.3\ \text{ps})$ and (b) $(\tau_2, \tau_i) = (100\ \text{ps}, 30\ \text{ps})$. Thick-blue-solid, red-dashed-filled, and black-dotted lines depict $\rho_{22}(t, 0) - \rho_{11}(t, 0)$ from the numerical solution of Eqs. (1)–(16) and numerical integration of Eqs. (21) and (25), respectively. Three downward green arrows chronologically indicate three key temporal instants, namely, $\tau_i - u\tau_p$, τ_i, and $\tau_i - u\tau_p + \tau_2 \ln 2$. The gain duration of $I(t, z) > 0$ is about $\tau_2 \ln 2$. Other parameters are $(r, n_p, \tau_p, \sigma) = (2\ \mu\text{m}, 30 \times 10^{12}, 60\ \text{fs}, 3.336 \times 10^{-23}\ \text{m}^2)$.

The dynamics of ρ_{22} obey $\partial_t \rho_{22} = \sigma J_p \rho_{00} - \Gamma \rho_{22}$, whose solution reads

$$\rho_{22}(t) \approx \frac{n_p \sigma}{\pi^{3/2} r^2 \tau_p} \exp\left(-\Gamma t - \frac{n_p \sigma}{2\pi r^2}\right) \times \int_0^t \exp\left[\Gamma s - \frac{n_p \sigma}{2\pi r^2} \text{erf}\left(\frac{s - \tau_i}{\tau_p}\right) - \left(\frac{s - \tau_i}{\tau_p}\right)^2\right] ds. \tag{21}$$

Invoking the conservation of population $\sum_{i=1}^{3} \rho_{ii}(t, z) = 1$ one gets ρ_{11}. A careful comparison confirms that Eq. (21) is equivalent to the numerical solution of the complete Eqs. (1)–(16). When $\tau_p < \tau_2$, we can obtain the following approximate solutions:

$$\rho_{22}(t, z) \approx [1 - \rho_{00}(t)] e^{-\Gamma\left(t - \tau_i - \frac{z}{c} + u\tau_p\right)}, \tag{22}$$

$$\rho_{11}(t, z) \approx [1 - \rho_{00}(t)]\left[1 - e^{-\Gamma\left(t - \tau_i - \frac{z}{c} + u\tau_p\right)}\right], \tag{23}$$

$$u = 2 + \frac{e\pi^{3/2} r^2}{n_p \sigma}\left(1 - \sqrt{1 + \frac{4 n_p \sigma}{e\pi^{3/2} r^2}}\right), \tag{24}$$

where $u\tau_p$ corresponds to $\partial_t^2 \rho_{00}(t)|_{t = u\tau_p} = 0$ when the maximum consumption rate of ρ_{00} by J_p occurs, and e is Euler's number. One can also obtain the approximate population inversion $I(t, z) = \rho_{22}(t, z) - \rho_{11}(t, z)$:

$$I(t, z) \approx [1 - \rho_{00}(t, z)]\left[2e^{-\Gamma\left(t - \tau_i - \frac{z}{c} + u\tau_p\right)} - 1\right]. \tag{25}$$

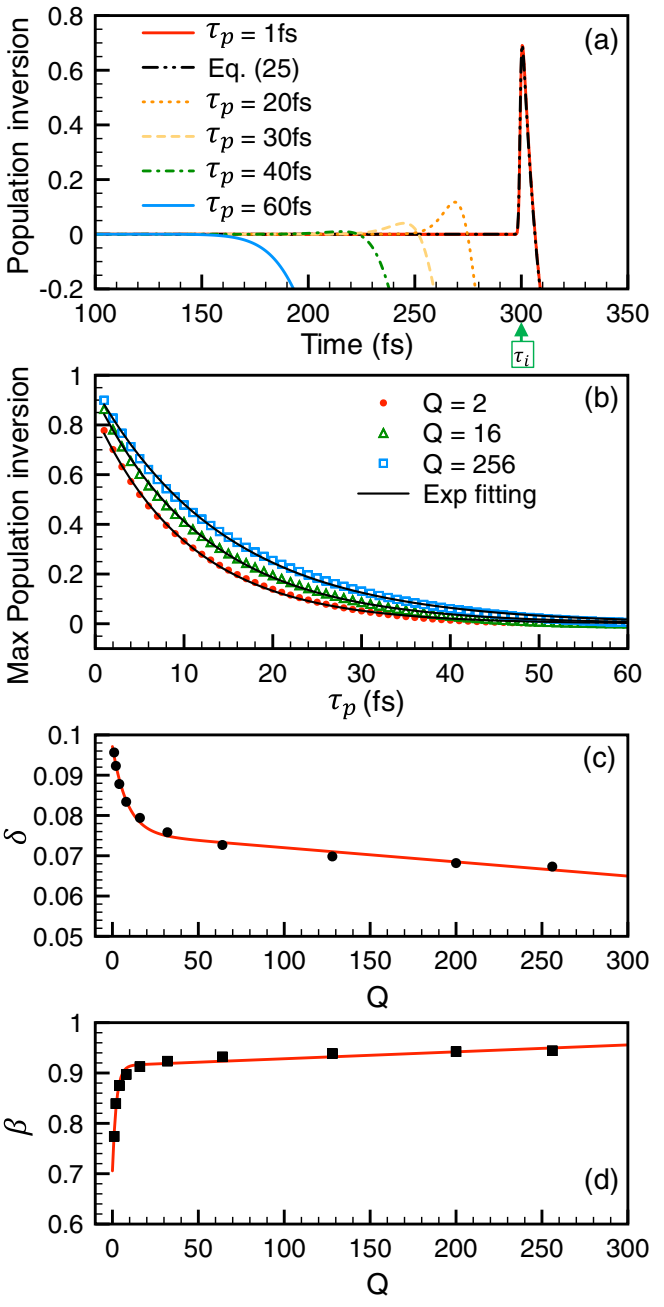

FIG. 3. (a) Population inversion $I(t, z = 0)$ for $(\tau_2, \tau_i) = (10\ \text{fs}, 300\ \text{fs})$ and a range of J_p pulse duration based on the XFEL parameter, namely, $\tau_p = 1$ fs (red solid line), $\tau_p = 20$ fs (orange dotted line), $\tau_p = 30$ fs (yellow dashed line), $\tau_p = 40$ fs (green dashed-dotted line), and $\tau_p = 60$ fs (blue dashed-dashed-dotted-dotted line). Black dashed-dotted-dotted line is Eq. (25). Other parameters are $(n_p, \tau_p, r, \sigma) = (Q T_p \times 10^{12},\ T_p\ \text{fs},\ 2\mu\text{m},\ 3.336 \times 10^{-23}\ \text{m}^2)$ and $Q = 1$. Upward green arrow indicates τ_i. (b) The max population inversion as a function of T_p for $Q = 2$ (red dots), $Q = 16$ (green triangles), and $Q = 256$ (blue squares). Black solid lines are $\beta e^{-\delta T_p}$ fittings. (c) Q-dependent δ. (d) Q-dependent β.

Figure 2 demonstrates the comparison between the numerical solution of the complete Eqs. (1)–(16), the numerical integration of Eq. (21), and the analytical solution of Eq. (25) for $\tau_2 = 1$ and $\tau_2 = 100$ ps. This plainly demonstrates the consistency between the three methods. When the timescale of τ_2 is small and approaching τ_p, the effect caused by the leading edge of the J_p pulse becomes significant, i.e., the shift $u\tau_p$ of around 0.2 ps in Fig. 2(a). The peak value of $I(t,z)$ actually happens at about $\tau_i + \frac{z}{c} - u\tau_p$ instead of $\tau_i + \frac{z}{c}$. The temporal shift of $u\tau_p$, namely, the spacing between the first two downward green arrows, reveals that the subsequent emissions may overtake J_p. The excited atoms subsequently experience spontaneous decay and give a similar duration of $\tau_2 \ln 2$, i.e., the spacing between the first and third downward green arrows, for positive $I(t,z)$. This gain domain, e.g., [0.2 ps, 0.9 ps] in Fig. 2(a) and [30 ps, 98 ps] in Fig. 2(b), is the energy reservoir for ASE while outside the region $\Omega^{\pm}$ will be reabsorbed by atoms in the ground state. One can accordingly define the transient gain length $L_g = c\tau_p/2$ in the medium. The analysis of $I(t,z)$ is important for the understanding of the ASE gain curve, which will be performed in what follows.

In order to investigate the gain process of Ω^+, we further approximate

$$I(t,z) \approx \left[2e^{-\Gamma\left(t-\tau_i-\frac{z}{c}+u\tau_p\right)} - 1\right]\Theta\left(t - \tau_i - \frac{z}{c} + u\tau_p\right), \quad (26)$$

where Θ is the Heaviside unit step function, and solve the simplified equations $\partial_t \rho_{21}^+ = -\frac{i}{2}PI\Omega^+$ and $\partial_z \Omega^+ = i\eta\rho_{21}^+$. The integral of the former leads to $\rho_{21}^+(t,z) = -\frac{i}{2}P\int_0^t \Omega^+(\tau,z)I(\tau,z)d\tau$, which is then substituted into the latter. We arrive at

$$\begin{aligned}\partial_z\Omega^+(t,z) &= \frac{P\Gamma\alpha}{4L}\int_0^t \Omega^+(\tau,z)I(\tau,z)d\tau \\ &\approx \Omega^+(t,z)\frac{P\Gamma\alpha}{4L}\int_0^t I(\tau,z)d\tau. \end{aligned} \quad (27)$$

Neglecting $\partial_t\Omega^+$ in the wave equation is justified when Eq. (26) goes to the retarded time frame, namely, as a function of $t - \frac{z}{c}$ [43,47,54]. The additional factor P indicates the weighting of the forward emission. In the early stage, i.e., $\Gamma \gg |\Omega^+|$, spontaneous emission dominates, and so $P = 1/2$ is expected in the simplified equations because an atom has the equal chance for the forward/backward spontaneous emission. We further neglect the temporal structure of $\Omega^+(t,z)$ and extract it from the integrand of Eq. (27). The peak value of the output Ω^+ pulse in the end of the medium ($z = L$) reads

$$\begin{aligned}\Omega^+(L) &\approx \Omega_0^+ \exp\left\{\frac{P\Gamma\alpha}{4L}\int_0^L\int_{\tau_l}^{\tau_u} I(\tau,z)d\tau dz\right\} \\ &= \Omega_0^+ e^{\xi\alpha}. \end{aligned} \quad (28)$$

Here Ω_0^+ is given by Gaussian white noise, and $\tau_l = \tau_i + \frac{z}{v}$, $\tau_u = \tau_i + \frac{z}{c} - u\tau_p + \tau_2 \ln 2$. Because Ω^+ is always behind J_p and must stay in the gain interval $[\tau_l, \tau_u]$, where the population inversion $I > 0$, as demonstrated in Fig. 2, the gain factor 2ξ is then determined to be

$$\begin{aligned}2\xi = \frac{P}{4}\Bigg\{&\frac{L\Gamma}{v} - \frac{L\Gamma}{c} + 2u\tau_p\Gamma - 2 - \ln 4 \\ &- \frac{4cv}{(c-v)L\Gamma}e^{-u\tau_p\Gamma}\left[e^{\left(\frac{1}{c}-\frac{1}{v}\right)L\Gamma} - 1\right]\Bigg\}. \end{aligned} \quad (29)$$

The upper bound of 2ξ in Eq. (29) occurs when v approaches c, namely,

$$\lim_{v\to c} 2\xi = \frac{P}{2}(2e^{-u\tau_p\Gamma} + u\tau_p\Gamma - 1 - \ln 2), \quad (30)$$

which results in the maximum gain exponent. One can deduce the range of the group velocity v of the emitted light pulse as follows. Given the fact that the Ω^+ pulse propagates with group velocity v all the way behind J_p, thus $v < c$. Since the emitted light must stay in the gain domain illustrated in Fig. 2 when $I(t,z) > 0$, otherwise it will be reabsorbed, we have the gain condition $\tau_i + \frac{z}{c} \leqslant \tau_l \leqslant \tau_u$. This indicates that J_p produces population inversion at z during $[\tau_i + \frac{z}{c}, \tau_u]$, where we neglect the small correction of $u\tau_p$ in the lower bound, but Ω^+ passes through z at τ_l which must be within the above gain interval. The inverse of the gain condition leads to the range of v:

$$c \geqslant v \geqslant \frac{cL\Gamma}{L\Gamma + c\ln 2 - c\Gamma u\tau_p}. \quad (31)$$

We analyze the trajectory of the emitted pulse and observe that the group velocity v is initially smaller than c and gradually approaches c when the optical ringing effect occurs. While the acceleration mechanism remains an interesting theoretical topic to be studied, one can still use Eq. (30) to estimate the upper bound of the ASE gain exponent.

In view of the time structure of XFEL [49] and the recent XFEL-pumped laser [22], we investigate the pumping process with a variety of XFEL parameters [49]. Figure 3(a) illustrates the numerical solution of $I(t,0)$ for $\tau_2 = 10$ fs with a variety of τ_p. We use $(n_p, \tau_p, \tau_i, r) = (QT_p \times 10^{12}, T_p\ \text{fs}, 300\ \text{fs}, 2\ \mu\text{m})$ and $Q = 1$ to fix the amplitude of J_p at a constant $4.5 \times 10^{37}\ \text{s}^{-1}\,\text{m}^{-2}$ when varying T_p. The red solid line depicts the case for $\tau_p = 1$ fs, i.e., $T_p = 1$, in which J_p is short enough to generate population inversion between states $|2\rangle$ and $|1\rangle$ with a peak value of 0.69. As one can see, the analytical solution Eq. (25) (black dashed-dotted-dotted line) also matches the numerical integration of Eq. (21) (red solid line) as $\tau_p < \tau_2$. When $\tau_p \geqslant \tau_2$, the analysis of Eq. (21) becomes a complicated problem, and the competition between the σJ_p and Γ terms in Eq. (3) causes $I(t,z)$ to exhibit more complicated behavior. For long pumping pulses of $\tau_p = 20$ fs (orange dotted line), $\tau_p = 30$ fs (yellow dashed line), $\tau_p = 40$ fs (green dashed-dotted line), and $\tau_p = 60$ fs (blue dashed-dashed-dotted-dotted line), the τ_p-dependent reduction of population inversion is observed. Such a reduction is caused by the consumption of ρ_{00} by the leading edge of J_p whose pumping power is too weak to compete against the fast decay of state $|2\rangle$. The leading edge of J_p and the decay rate Γ turn the medium transparent before the arrival of the peak of J_p. Figures 3(b) and 3(c) show that the increase of the amplitude of J_p slightly eases the reduction of population inversion due to the leading edge of J_p. In Fig. 3(b) we use $Q = 2$ (red dots), $Q = 16$ (green triangles), and $Q = 256$ (blue squares)

to demonstrate the effect of increasing the J_p amplitude on the maximum population inversion as a function of T_p. The black solid lines are $\beta e^{-\delta T_p}$ fittings. The Q dependent δ and β are respectively depicted in Figs. 3(c) and 3(d). As one can see in Fig. 3(c), in the Q domain of [1, 300], δ ranges between 0.07 and 0.1, corresponding to a variety of τ_p between 10 and 15 fs. When τ_p is shorter than this range, transient population inversion can be built up, and this results in a noticeable gain of $\Omega^{\pm}$. For $\tau_p > 40$ fs, population inversion is suppressed and the gain of $\Omega^{\pm}$ becomes negligible. Consequently, the temporal structure of a pumping pulse plays a more critical role than J_p amplitude does when τ_p and τ_2 are in a similar timescale. When τ_p is too long, the pumping capability of a J_p pulse will degrade. The rapid decrease of δ in Fig. 3(c) and the quick increase of β in Fig. 3(d) for $Q < 20$ suggest that there is an efficient choice of J_p amplitude to optimize the generation of population inversion. It is worth mentioning that the red solid fitting curves in Figs. 3(c) and 3(d) are in the form of $a + be^{-fQ} + gQ$, where a, b, f, and g are some fitting constants, which may provide useful information for future analytical study of $I(t, z)$.

IV. NUMERICAL RESULTS

Here we turn to the discussion of the numerical solution of Eqs. (1)–(16). Figure 4 demonstrates the results of (r, n_p, τ_p, τ_2) = (2 μm, 30×10^{12}, 60 fs, 1 ps), and Fig. 5 shows that of (r, n_p, τ_p, τ_2) = (2 μm, 30×10^{12}, 60 fs, 100 ps). Figures 4(a) and 5(a) depict the probability of forward emission $\int_{-\infty}^{\infty} |\Omega^+(t, L)|dt \geqslant \frac{\pi}{2}$ among 1000 realizations of simulation at each point of (L, n). Figures 4(b) and 5(b) depict that of backward emission $\int_{-\infty}^{\infty} |\Omega^-(t, 0)|dt \geqslant \frac{\pi}{2}$. In the forward emission for both $\tau_2 = 1$ ps and $\tau_2 = 100$ ps, the growth of the area of Ω^+ and its gain are observed when either the length of the medium L or the density of the medium n increases. However, for backward emission, the similar tendency only occurs when $\tau_2 = 100$ ps but is absent for $\tau_2 = 1$ ps. Figure 4(b) reveals that no matter how one changes the parameters of a gain medium, the backward pulse area $\int_{-\infty}^{\infty} |\Omega^-(t, 0)|dt$ is always negligible. This forward-backward asymmetry is discussed in Sec. V.

In both Figs. 4(a) and 5(a) there are five data sets marked as **c** (L, n) = (0.25 mm, 2.25×10^{14} mm^{-3}), **d** (0.5 mm, 1×10^{14} mm^{-3}), **e** (0.5 mm, 2.25×10^{14} mm^{-3}), **f** (0.5 mm, 3.5×10^{14} mm^{-3}), and **g** (0.75 mm, 2.25×10^{14} mm^{-3}). Average temporal intensity based on Eq. (17), average spectral intensity calculated by Eq. (18), and a photon number histogram of five chosen points are respectively demonstrated by ($\mathbf{x} - 1$), ($\mathbf{x} - 2$), and ($\mathbf{x} - 3$) of Figs. 4 and 5, where $\mathbf{x} \in \{\mathbf{c}, \mathbf{b}, \mathbf{e}, \mathbf{f}, \mathbf{g}\}$. When scanning parameters through either path **c**-**e**-**g** of lengthening the gain medium with constant density or **d**-**e**-**f** of densifying the gain medium for a given length, we observe that the pulse area becomes high and the occurrence of optical ringing and spectral splitting becomes significant. The typical $|\Omega^+(t, L)|^2$ values of single realization are illustrated by the insets of Fig. 4($\mathbf{x} - 1$). One can see that the optical ringing effect happens in the $\int_{-\infty}^{\infty} |\Omega^+(t, L)|dt \geqslant \frac{\pi}{2}$ region. The shortening of the $\Omega^+(t, L)$ pulse duration is accompanied by the widening of spectral splitting. The delay time between the peak of $J_p(t, L)$ and the peak of $\Omega^+(t, L)$ also becomes short, namely, speedup emission. For a better visualization, we indicate the peak instant of $J_p(t, L)$ by gray dashed lines in Fig. 4($\mathbf{x} - 1$), and it is very close to $t = 0$ in Fig. 5($\mathbf{x} - 1$) of a longer timescale. We demonstrate the time delay histogram of forward emission for $\tau_2 = 1$ ps in the insets of Fig. 4($\mathbf{x} - 3$). One can see that the most probable delay time is shifting to small value, and its fluctuation amplitude becomes ten times wider when the probability of $\int_{-\infty}^{\infty} |\Omega^+(t, L)|dt \geqslant \frac{\pi}{2}$ increases. Moreover, Fig. 4($\mathbf{x} - 3$) and Fig. 5($\mathbf{x} - 3$) show that the photon number histogram of the emitted $\Omega^+(t, L)$ spreads from left to right and gradually peaks at a certain large photon number. As also revealed by Fig. 4($\mathbf{x} - 3$) and Fig. 5($\mathbf{x} - 3$), the fluctuation amplitude of the photon number is also getting wide when the system goes to a high optical depth region. The $\langle I^-(t)\rangle$ and backward photon number histogram are illustrated in the Fig. 5($\mathbf{x} - 1$) inset and Fig. 5($\mathbf{x} - 3$) inset, respectively. Both share the same tendency with the forward one. The above features suggest that $\Omega^{\pm}$ experiences a certain transition [9,41,42] around the boundary of $\int_{-\infty}^{\infty} |\Omega^+(t, L)|dt = \frac{\pi}{2}$ and $\int_{-\infty}^{\infty} |\Omega^-(t, 0)|dt = \frac{\pi}{2}$ which is associated with Rabi oscillation. For $\tau_2 = 10$ fs, our numerical simulation shows that the population inversion is not produced by J_p when $\tau_p > 30$ fs. This confirms the analysis demonstrated in Fig. 3(a) using the integral approach. Figure 6 illustrates the results utilizing (r, n_p, τ_p, τ_2) = (2 μm, 10^{14}, 24 fs, 10 fs). Because the backward emission is negligible in this case, we only depict the probability of forward emission in Fig. 6(a). The three data sets are marked as **b** (L, n) = (0.2 mm, 6.5×10^{14} mm^{-3}), **c** (0.3 mm, 9.5×10^{14} mm^{-3}), and **d** (0.44 mm, 1.48×10^{15} mm^{-3}), and their corresponding spectra of $\Omega^+(t, L)$ are given in Figs. 6(b), 6(c), and 6(d), respectively. When moving to the top right along path **b**-**c**-**d**, the spectrum is getting split. This reflects the slightly oscillatory behavior damped by the high decay rate in the time domain, and a similar transition also happens at around $\int_{-\infty}^{\infty} |\Omega^+(t, L)|dt = \frac{\pi}{2}$ and $\int_{-\infty}^{\infty} |\Omega^-(t, 0)|dt = \frac{\pi}{2}$.

In order to quantify the observed transition, we collect $|\Omega^+(t, L)|^2$ and $|\Omega^-(t, 0)|^2$ for each contour in Figs. 4 and 5 and analyze them by finding the α power law for the averaged peak intensity and for the averaged delay time. In Figs. 7(a), 8(a), and 8(b) the black circles depict the α-dependent peak intensity. In Figs. 7(b), 8(c), and 8(d) the black squares demonstrate the α-dependent delay time. The blue dashed lines are fitting curves for $\alpha \leqslant 500$, green dotted line for $500 < \alpha < 1200$, and red solid lines for $\alpha > 1200$. In Figs. 7 and 8 the domain $500 < \alpha < 1200$ and $700 < \alpha < 1500$ are obviously the watershed of power law, respectively. To the left of the watershed the peak intensity exhibits exponential growth with a constant delay time of 0.551 ps for $\tau_2 = 1$ ps and that of about 65 ps for $\tau_2 = 100$ ps, which typically results from ASE. The upper bound of the ASE gain exponent of 0.055 and that of 0.076 are given by Eq. (30) for $\tau_2 = 1$ ps and $\tau_2 = 100$ ps, respectively. Both are in the same order of magnitude with the fitting value of 0.022 [blue dashed line in Figs. 7(a), 8(a), and 8(b)]. However, to the right of the watershed the peak intensity is proportional to α^2, and the delay time behaves as the typical form of $\tau_D \propto \alpha^{-1}[\frac{1}{2}\ln(2\pi\alpha)]^2$ [2,3,59]. The former corresponds to the collective emission and the latter reflects the needed time for building up coherence from noise [2,3], which are both signatures of superfluorescence. It is worth mentioning that the typical form of superfluorescence

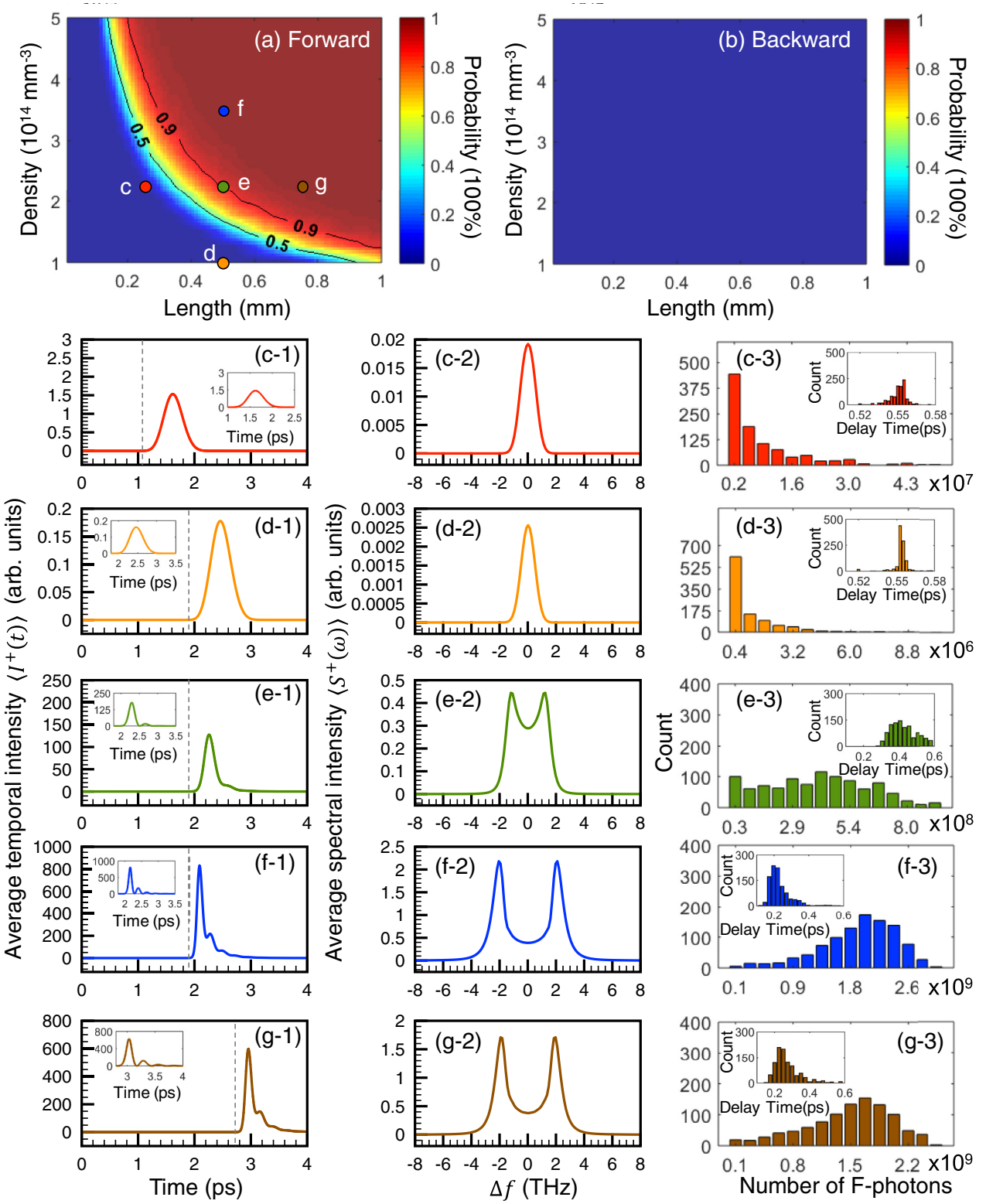

FIG. 4. Probability of (a) forward $\int_{-\infty}^{\infty}|\Omega^+(t,L)|dt \geqslant \frac{\pi}{2}$ and that of (b) backward $\int_{-\infty}^{\infty}|\Omega^-(t,0)|dt \geqslant \frac{\pi}{2}$ as a function of (L, n) among 1000 realizations with Gaussian random noise for $(r, n_p, \tau_p, \tau_2) = (2\ \mu\text{m}, 30\times10^{12}, 60\text{ fs}, 1\text{ ps})$. Five data sets marked as **c** $(L, n) = (0.25\text{ mm}, 2.25\times10^{14}\text{ mm}^{-3})$, **d** $(0.5\text{ mm}, 1\times10^{14}\text{ mm}^{-3})$, **e** $(0.5\text{ mm}, 2.25\times10^{14}\text{ mm}^{-3})$, **f** $(0.5\text{ mm}, 3.5\times10^{14}\text{ mm}^{-3})$ and **g** $(0.75\text{ mm}, 2.25\times10^{14}\text{ mm}^{-3})$ in (a) are picked up to show the transition from amplified spontaneous emission to superfluorescence of Ω^+. The corresponding average temporal intensity, average spectral intensity, and photon number histogram of each chosen point are respectively illustrated by $(\mathbf{x}-1)$, $(\mathbf{x}-2)$, and $(\mathbf{x}-3)$, where $\mathbf{x}\in\{\mathbf{c},\mathbf{b},\mathbf{e},\mathbf{f},\mathbf{g}\}$. Gray dashed lines in (**c**-1)–(**g**-1) indicate instants when J_p leaves the medium. Insets in (**c**-1)–(**g**-1) and (**c**-3)–(**g**-3) demonstrate the typical $|\Omega^+(t,L)|^2$ of a single realization and delay time histogram of forward emission at each chosen set of parameters, respectively.

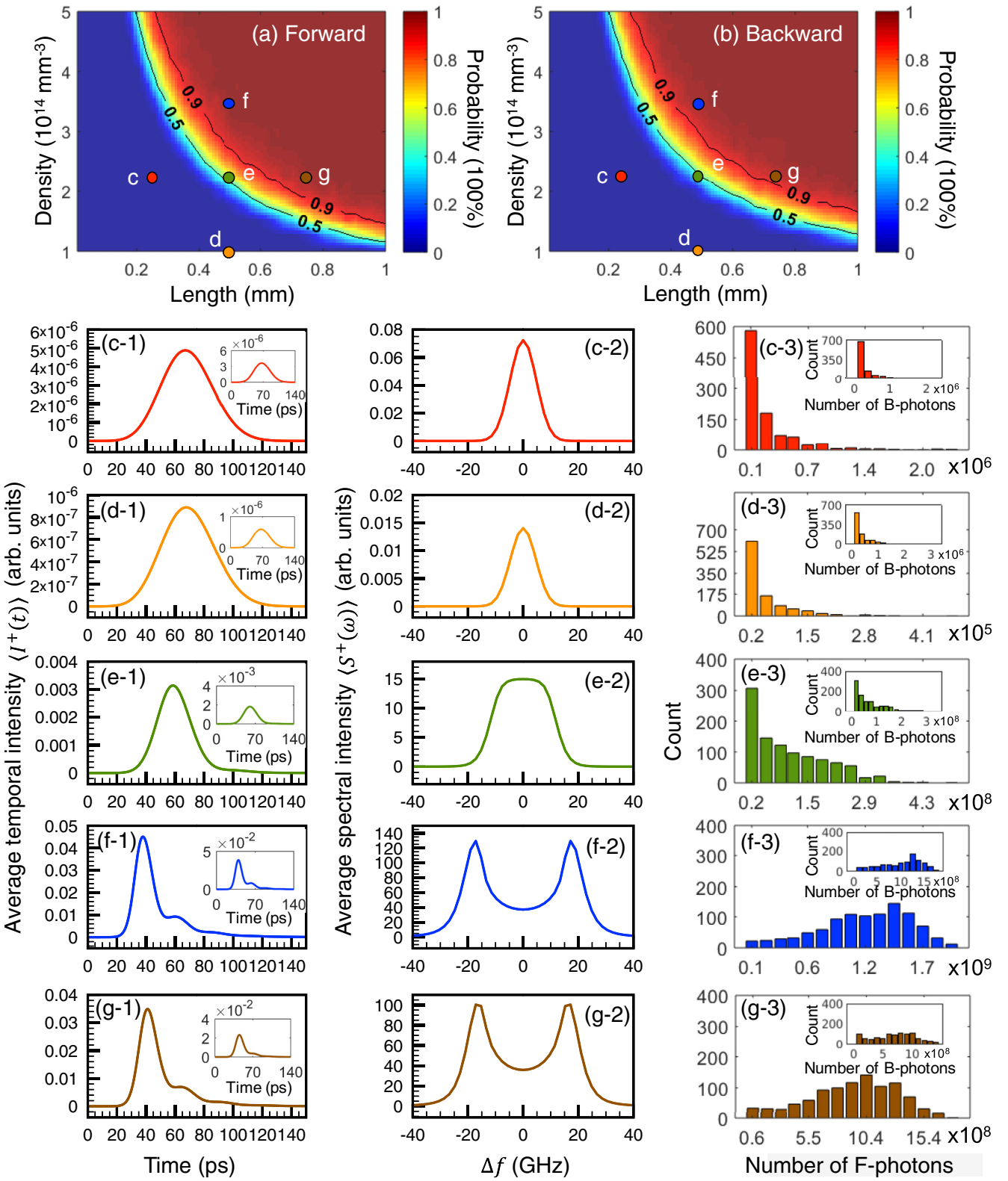

FIG. 5. Probability of (a) forward $\int_{-\infty}^{\infty}|\Omega^+(t,L)|dt \geqslant \frac{\pi}{2}$ and that of (b) backward $\int_{-\infty}^{\infty}|\Omega^-(t,0)|dt \geqslant \frac{\pi}{2}$ as a function of (L, n) among 1000 realizations with Gaussian random noise for $(r, n_p, \tau_p, \tau_2) = (2\ \mu\text{m}, 30\times10^{12}, 60\text{ fs}, 100\text{ ps})$. Five data sets, marked as **c** $(L, n) = (0.25\text{ mm}, 2.25\times10^{14}\text{ mm}^{-3})$, **d** $(0.5\text{ mm}, 1\times10^{14}\text{ mm}^{-3})$, **e** $(0.5\text{ mm}, 2.25\times10^{14}\text{ mm}^{-3})$, **f** $(0.5\text{ mm}, 3.5\times10^{14}\text{ mm}^{-3})$, and **g** $(0.75\text{ mm}, 2.25\times10^{14}\text{ mm}^{-3})$ in (a) and (b), are chosen for showing the transition from amplified spontaneous emission to superfluorescence. The corresponding average temporal intensity, average spectral intensity, and photon number histogram of the forward emission at each chosen point are respectively illustrated by $(\mathbf{x}-1)$, $(\mathbf{x}-2)$, and $(\mathbf{x}-3)$, where $\mathbf{x}\in\{\mathbf{c},\mathbf{b},\mathbf{e},\mathbf{f},\mathbf{g}\}$. The corresponding average temporal intensity and photon number histogram of the backward emission are illustrated in the insets of (**c**-1)–(**g**-1) and those of (**c**-3)–(**g**-3), respectively.

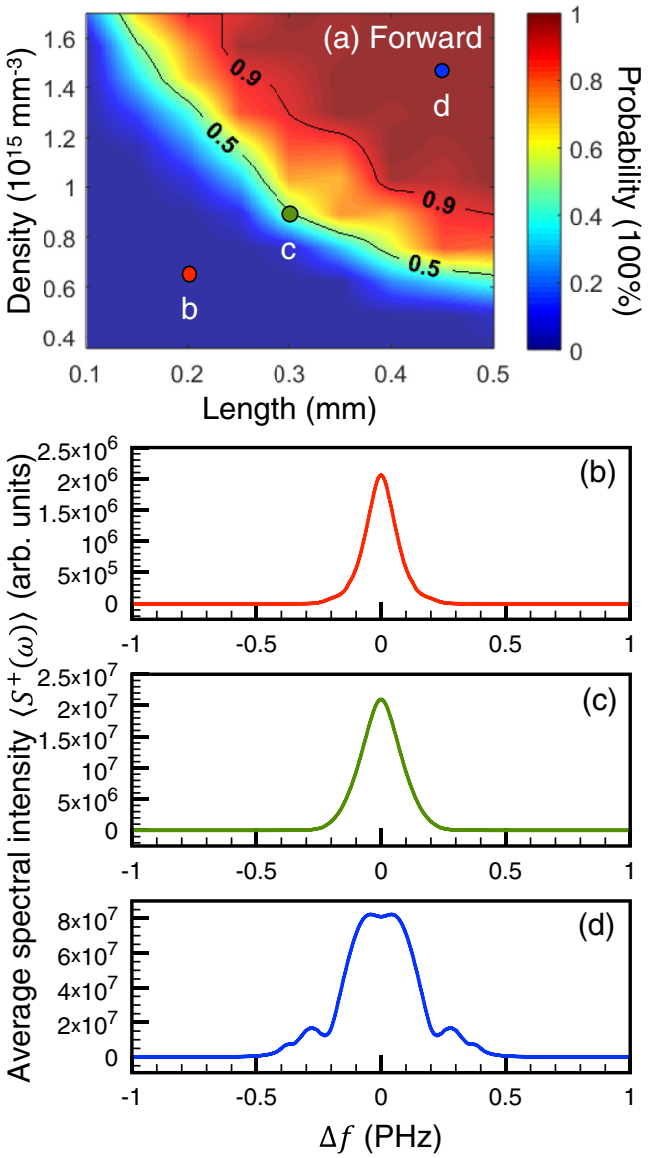

FIG. 6. (a) Probability of $\int_{-\infty}^{\infty}|\Omega^+(t,L)|dt \geqslant \frac{\pi}{2}$ occurs as a function of (L, n) in forward direction among 1000 realizations with Gaussian random noise for $(r, n_p, \tau_p, \tau_2) = (2\ \mu\text{m}, 10^{14}, 24\ \text{fs}, 10\ \text{fs})$. $\alpha \simeq 1760$ for probability of 50%. The average spectral intensity of five data sets, marked as **b** $(L,\ n) = (0.2\ \text{mm},\ 6.5\times10^{14}\ \text{mm}^{-3})$, **c** $(0.3\ \text{mm},\ 9.5\times10^{14}\ \text{mm}^{-3})$, **d** $(0.44\ \text{mm},\ 1.48\times10^{15}\ \text{mm}^{-3})$, are chosen for showing the transition from amplified spontaneous emission to superfluorescence of Ω^+.

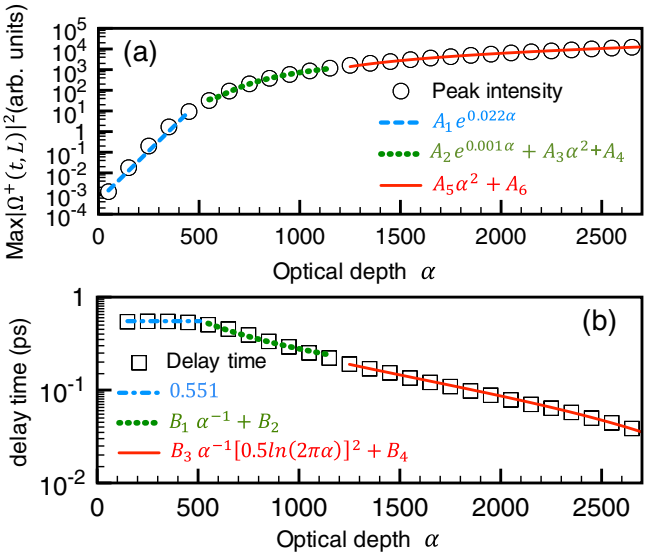

FIG. 7. α-dependent (a) peak intensity and (b) delay time of the emitted pulse $|\Omega^+(t,L)|^2$ for $\tau_2 = 1$ ps. Black circles and black squares respectively represent peak intensity and delay time from numerical solutions of $|\Omega^+(t,L)|^2$. Each color line illustrates a fitting curve in the corresponding α domain. All parameters are those used in Fig. 4. The fitting coefficients are $(A_1, A_2, A_3, A_4, A_5, A_6) = (4.72\times10^{-4}, -5.42\times10^{3}, 8.65\times10^{-3}, 6.82\times10^{3}, 1.96\times10^{-3}, -1.66\times10^{3})$ and $(B_1, B_2, B_3, B_4) = (2.97\times10^{2}, -1.86\times10^{-2}, 2.11\times10, -1.5\times10^{-1})$.

delay time deviates from the numerical values when $\alpha < 1200$ and $\alpha < 1500$ for $\tau_2 = 1$ ps and $\tau_2 = 100$ ps, respectively. In the watershed domain, the green dotted line in Figs. 7(a), 8(a), and 8(b) indicate that the peak intensity behaves as a superposition of exponential growth and α^2. This tendency reveals that a transition does happen from one emission mechanism to another [9,41]. The present results also suggest that the optical depth α plays the key role for a transition from ASE to SF. This transition happens at the boundary where Rabi oscillation also starts to occur. The validity of one-dimensional simulation is associated with the Fresnel number condition $\mathbf{F} = \frac{\pi r^2}{L\lambda} \approx 1$. Otherwise, one has to deal with full three-dimensional wave propagation in simulations for the transverse effect of diffraction [3], which consumes a lot of computational time and power, especially for the ensemble average. To avoid such heavy computation, we have compared averaged results due to different values of n and L for $nL =$ constant, i.e., $\alpha =$ constant, in our model and do not observe any significant difference. Therefore, one could take advantage of the α-dependent features and effectively use a system which fulfils the Fresnel condition with the same α.

Given that the boundary between ASE and SF may occur when $\int_{-\infty}^{\infty}\Omega(t)dt = \frac{\pi}{2}$, we here estimate the photon number of an emitted $\frac{\pi}{2}$ pulse. For simplicity, we use a Gaussian pulse such that $\int_{-\infty}^{\infty}\Omega\exp[-(\frac{t}{\kappa\tau_2})^2]dt \approx \Omega\sqrt{\pi}\kappa\tau_2 = \frac{\pi}{2}$, where $\kappa\tau_2$ is the duration of the emitted pulse, and $\kappa = \ln 2$ given by the duration of positive population inversion as illustrated in Fig. 2. One can therefore obtain $\Omega \approx \frac{\sqrt{\pi}}{2\tau_2\ln 2}$. In view of the fact that the integral of laser intensity equals the energy of n_e photons, $\frac{1}{2}c\varepsilon_0\pi r^2\int_{-\infty}^{\infty}\frac{\hbar^2}{d^2}|\Omega(t)|^2dt = n_e\hbar\omega$, which results in the number of photons emitted by $|2\rangle \rightarrow |1\rangle$ transition $n_e \approx \frac{\hbar c\varepsilon_0\pi^{5/2}r^2}{8\sqrt{2}\omega d^2\ln 2}\Gamma$. By substituting $c = \omega\lambda/(2\pi)$, the spontaneous decay rate $\Gamma = \frac{d^2\omega^3}{3\pi\varepsilon_0\hbar c^3}$ and d the transition dipole moment of $|1\rangle \rightarrow |2\rangle$ transition, we obtain

$$n_e \approx \frac{\pi^{\frac{7}{2}}r^2}{6\sqrt{2}\lambda^2\ln 2}. \tag{32}$$

This suggests that n_e of a $\frac{\pi}{2}$ pulse mainly depends on the ratio of r to λ. In the present cases, $n_e = 1.75\times10^7$ is very close to our numerical result of 3.24×10^7.

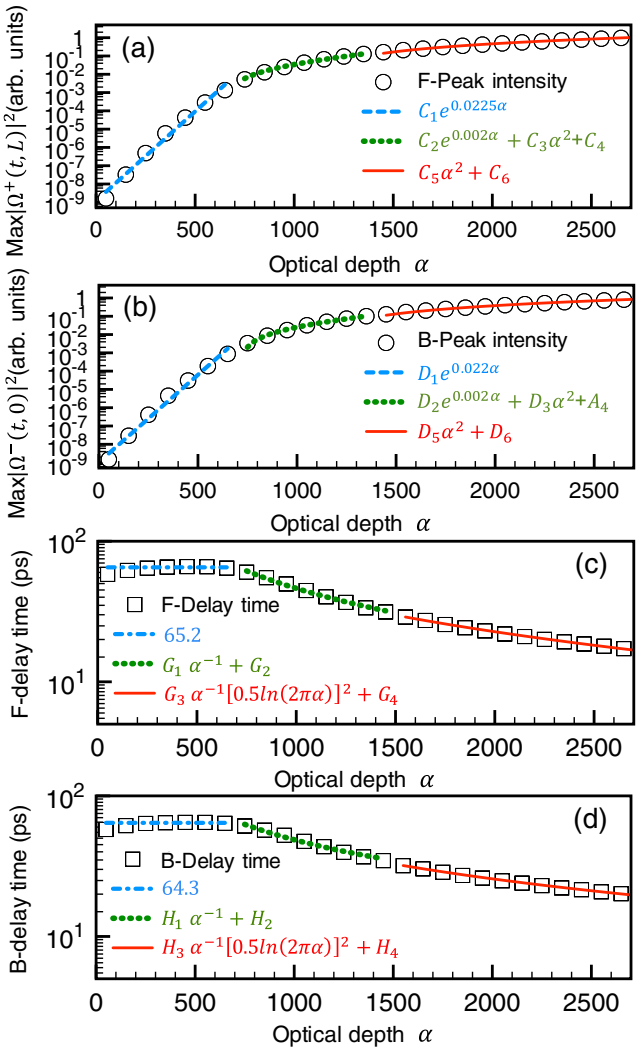

FIG. 8. α-dependent peak intensity of (a) forward $|\Omega^+(t,L)|^2$ and (b) backward $|\Omega^-(t,0)|^2$ for $\tau_2 = 100$ ps. α-dependent delay time of the emitted pulse (c) $|\Omega^+(t,L)|^2$ and (d) $|\Omega^-(t,0)|^2$. Black circles and black squares respectively represent peak intensity and delay time from numerical solutions. Each color line illustrates a fitting curve in the corresponding α domain. All parameters are those used in Fig. 5. The fitting coefficients are $(C_1, C_2, C_3, C_4, C_5, C_6) = (1.21 \times 10^{-9},\ 0.021,\ -7.38 \times 10^{-8},\ -0.05,\ 1.7 \times 10^{-7},\ -0.22)$, $(D_1, D_2, D_3, D_4, D_5, D_6) = (1.05 \times 10^{-9},\ 0.016,\ -5.46 \times 10^{-8},\ -0.04,\ 1.41 \times 10^{-7},\ -0.18)$, $(G_1, G_2, G_3, G_4) = (4.58 \times 10^4,\ 3.96 \times 10^{-1},\ 2.5 \times 10^3,\ -5.258)$, and $(H_1, H_2, H_3, H_4) = (4.2 \times 10^4,\ 6.77,\ 2.53 \times 10^3,\ -2.47)$.

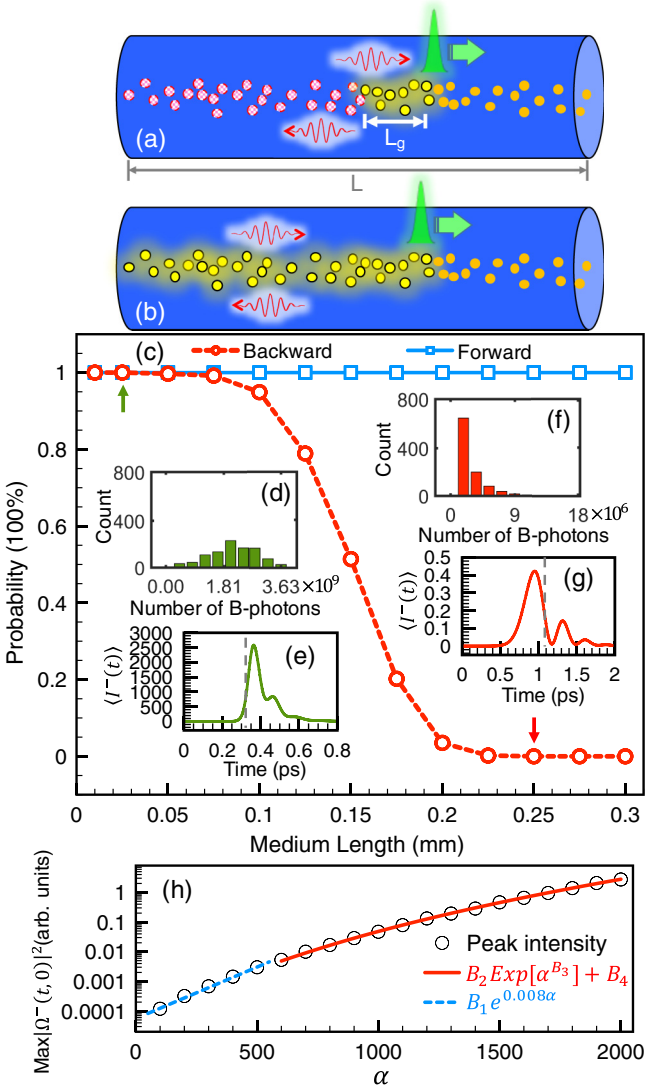

FIG. 9. Forward and backward asymmetry and length-induced backward transition. All particles are initially prepared in state $|0\rangle$ (orange-filled circles). (a) As $L_g < L$, pumped particles remain in the excited state $|2\rangle$ (yellow dots) for only a short distance behind the pumping pulse (green-right-moving Gaussian), and others decay to state $|1\rangle$ (red shaded circles). (b) Case when $L_g > L$. (c) Probability of forward $\int_{-\infty}^{\infty} |\Omega^+(t,L)|dt \geqslant \frac{\pi}{2}$ (blue solid line) and that of backward $\int_{-\infty}^{\infty} |\Omega^-(t,0)|dt \geqslant \frac{\pi}{2}$ (red dashed line) as a function of L among 1000 realizations for $(\tau_2, \alpha) = (1$ ps, $1500)$. Other parameters are the same as those used in Fig. 4. (d) Backward photon number histogram and (e) $\langle I^-(t)\rangle$ for $L = 0.025$ mm (indicated by green upward arrow). (f) Backward photon number histogram and (g) $\langle I^-(t)\rangle$ for $L = 0.25$ mm (indicated by red downward arrow). Gray dashed lines indicate instants when J_p leaves the medium. (h) α-dependent average backward peak intensity for $L = 0.25$ mm. Fitting parameters $(B_1, B_2, B_3, B_4) = (5.57 \times 10^{-5},\ 6.07 \times 10^{-8},\ 3.78 \times 10^{-1}, 4.52 \times 10^{-4})$.

V. LENGTH-INDUCED BACKWARD TRANSITION

We turn to investigate the forward-backward asymmetry demonstrated in Figs. 4(a) and 4(b) and its relation with L_g and L. Figure 9(a) shows that the regions which sandwich the small gain area (filled with yellow shaded circles) cause an asymmetric environment for light propagating forwards and backwards. For $L_g < L$ there is always a gain medium ($\rho_{22} > \rho_{11}$) ahead for light propagating forward but an absorption medium ($\rho_{22} < \rho_{11}$) for the backward radiation. This is one of reasons why backward emission is often absent in a swept pumping system. In contrast, Fig. 9(b) reveals that choosing a system with $L_g > L$ will lead to symmetric behavior for both directions. As a result, the increase of Ω^- gain and events of $\int_{-\infty}^{\infty} |\Omega^-(t,0)|dt \geqslant \frac{\pi}{2}$ are observed for $\tau_2 = 100$ ps in Fig. 5(b).

Given $L_g = 0.15$ mm for $\tau_2 = 1$ ps, as demonstrated in Fig. 2(a), the backward superfluorescence is anticipated to show up as $L < 0.15$ mm, but not when $L > 0.15$ mm. In what follows we use the constant $\alpha = 1500$ and the same parameters used in Fig. 4 to demonstrate a length-induced backward ASE-SF transition in Fig. 9(c). The blue solid line and red dashed line respectively represent the probability of $\int_{-\infty}^{\infty} |\Omega^+(t, L)|dt \geqslant \frac{\pi}{2}$ and that of $\int_{-\infty}^{\infty} |\Omega^-(t, 0)|dt \geqslant \frac{\pi}{2}$ among 1000 realizations of simulation for each length. Figures 9(d) and 9(e) show a backward photon number histogram and $\langle I^-(t)\rangle$, respectively, for $L = 0.025$ mm, and Figs. 9(f) and 9(g) for $L = 0.25$ mm. J_p leaves the medium at the instants pointed out by gray dashed lines. As one would expect from Fig. 4(a), the forward probability remains 100% for the whole length range. However, the backward emission reveals five interesting features when shortening L across the critical value of $L_g = 0.15$ mm: (1) probability noticeably raises to 100%; (2) $\langle I^-(t)\rangle$ catches up J_p; (3) the backward light pulse exits the medium earlier than J_p does when $L \gtrsim L_g$, as depicted by Fig. 9(g); (4) the photon number histogram demonstrates a similar ASE-SF transition, as depicted in Figs. 4 and 5; (5) $\langle I^-(t)\rangle$ manifests optical ringing as illustrated by Fig. 9(g) (also in single cases). The above features support our picture of the length effect and are consistent with Fig. 2(a) and Eq. (25), which is the consequence of $J_p(t, 0)$ and τ_2. The tiny pulse peaks at $t = 1.3$ ps in Fig. 9(g) suggests that the backward emission from a region deeper than L_g is possible. In view that the backward pulse area for $L \gtrsim L_g$ in Fig. 9(c) is mostly smaller than $\pi/2$, one would expect it is in the low-gain and linear region. However, the optical ringing is never observed in the ASE region of Fig. 5, and so feature (5) raises the following question for backward emission. Why can small pulse area and optical ringing coexist in the range of $L_g \sim L$ but cannot in $L_g > L$? Since the backward pulse duration in Fig. 9(g) is shorter than τ_2 limited by L_g, a broadband small-area pulse envelope should also oscillate when propagating through a resonant medium of high optical depth [60]. This will not happen to forward ASE because the gain medium co-moves along with it, making forward ASE duration always comparable to τ_2, i.e., narrow band, as demonstrated in Figs. 4 and 5. Nevertheless, the nonoscillating ASE in Fig. 5 suggests there is a mechanism other than Ref. [60], namely, attenuating SF. Because $\alpha = 1500$ is very high, the backward emission can quickly grow into SF in the gain region and then enters the dissipative but still penetrable area such that small pulse area and optical ringing can coexist in the range of $L_g \sim L$. In Fig. 9(h) we depict average backward peak intensity as a function of α by varying n but fixing $L = 0.25$ mm. Each point is also an average over 1000 realizations of simulation. The fitting shows that $\Omega^-(t, 0)$ does experience a transition at around $\alpha = 500$ and manifests nonlinear evolution lower than α^2 dependence. In contrast, the forward light behaves identically as that in Fig. 7. Similar study for $L = 0.025$ mm also shows an identical ASE-SF transition for both forward and backward emissions. Our backward study suggests that (I) a triggered small-area ASE by an external seeding pulse shorter than τ_2 may lead also to an oscillating ASE in both forward and backward direction due to the mechanism of Ref. [60], and (II) the transverse pumping may ease the forward-backward asymmetry.

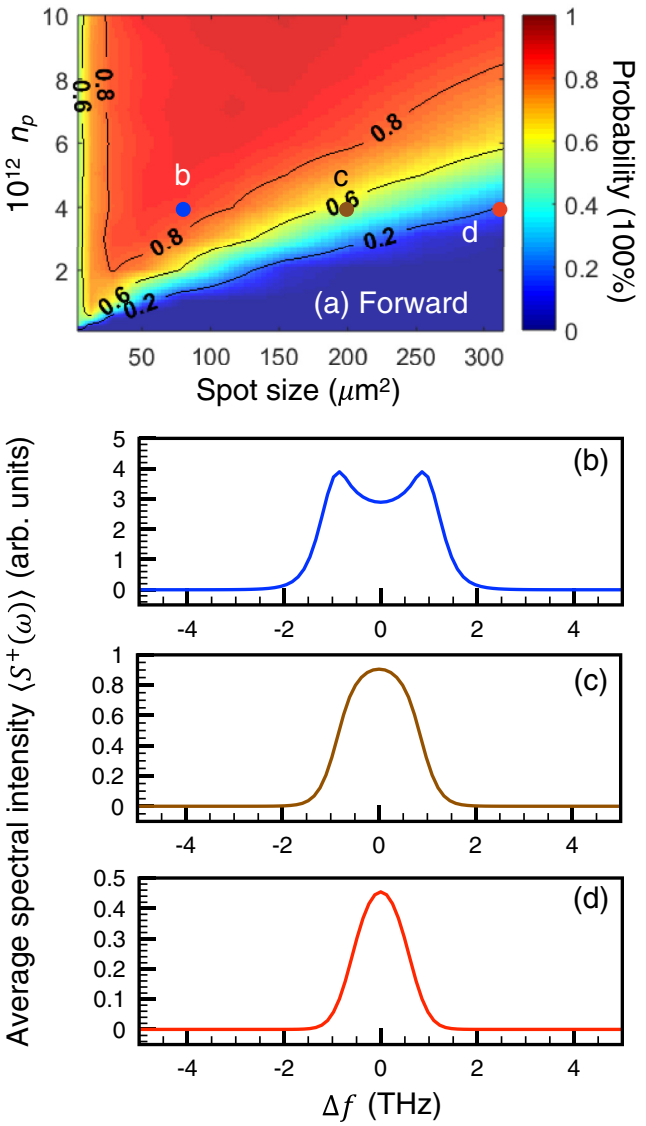

FIG. 10. (a) Probability of superfluorescence occurs as a function of $(\pi r^2, n_p)$ in forward direction among 1000 realizations for $(L, n, \tau_2) = (0.16$ mm, 5×10^{14} mm^{-3}, 1 ps) with Gaussian random noise. Three data sets, marked as **b** (78.54 μm^2, 4×10^{12}), **c** (201.06 μm^2, 4×10^{12}), **d** (314.16 μm^2, 4×10^{12}) in (a), are chosen for showing the transition from amplified spontaneous emission to superfluorescence. The corresponding average spectra are respectively illustrated in (b), (c), and (d).

VI. TRANSITION INDUCED BY XFEL J_p LASER PARAMETERS

It is a natural question to ask whether one could manipulate Ω^+ by changing the J_p laser [4,17,18,54] based on the XFEL parameter [49]. In Fig. 10(a) we demonstrate the probability of the occurrence of $\int_{-\infty}^{\infty} |\Omega^+(t, L)|dt \geqslant \frac{\pi}{2}$ as a function of $(\pi r^2, n_p)$. In our simulation, the pumping photon flux is affected by both r and n_p as denoted by Eq. (13), and the Gaussian white noise also depends on r as indicated by Eq. (16). Given the short lifetime $\tau_2 = 1$ ps, gain growth happens only to the forward emissions. We use $(L, n, \tau_2) = (0.16$ mm, 5×10^{14} mm^{-3}, 1 ps) to numerically

solve Eqs. (1)–(16) for 1000 realizations of simulation at each combination of J_p laser spot size and photon number. The three data sets are marked as **b** (78.54 μm^2, 4×10^{12}), **c** (201.06 μm^2, 4×10^{12}), and **d** (314.16 μm^2, 4×10^{12}) in Fig. 10(a). Their averaged spectra based on Eq. (18) is respectively demonstrated in Figs. 10(b), 10(c), and 10(d). When scanning parameters through the **b**-**c**-**d** path of shrinking J_p spot size and fixing n_p, the occurrence of spectral splitting also becomes obvious. As a consequence, one can manipulate the properties of emitted $\Omega^{\pm}$ not only by changing the parameters of the gain medium but also by altering that of the pumping laser J_p.

VII. SUMMARY

We have demonstrated the transition between ASE and SF in a three-level Λ-type system induced by the change of optical depth of a medium and by the alternation of pumping XFEL parameters, namely, focus spot size and pulse energy. A consistent picture of the transition from one region to another suggested by the Maxwell-Bloch equation is summarized in what follows. A pencil-shape gain medium is longitudinally and incoherently pumped by a short XFEL pulse, and then the inverted medium experiences spontaneous decay. Although the spontaneously emitted photons go to all directions, a small number of forward-emitted photons follow the XFEL pulse and enter the solid angle φ, as demonstrated in Fig. 1, within which photons may subsequently interact with other excited particles. The backward-emitted photons may also interact with the inverted particles or may be reabsorbed by the predecayed particles behind the gain region depending on $L_g \geqslant L$ or $L_g < L$, respectively (see Fig. 9). Due to the geometry, the forward-emitted light and the backward one, in the above former case, are both amplified along the long axis of the gain medium. As the pulse area approaches $\pi/2$, the ASE-SF transition starts to occur and results in, e.g., an optical ringing effect, spectral splitting, and the change in statistics behaviors as demonstrated in Figs. 4, 5, 7, and 8. We have investigated the pumping procedure in detail using the XFEL parameters and identified L_g and L as two key parameters making forward-backward asymmetry. Moreover, in the region of $L_g \gtrsim L$,we have also studied the length-induced backward transition. The present results demonstrate a controllable single-pass light source whose properties can be manipulated by parameters of a medium or those of a pumping XFEL.

ACKNOWLEDGMENTS

We thank Jason Payne for carefully reading our manuscript. Y.-H. K. and W.-T. L. are supported by the Ministry of Science and Technology, Taiwan (Grants No. MOST 107-2112-M-008-007-MY3 and No. MOST 107-2745-M-007-001-). W.-T. L. is also supported by the National Center for Theoretical Sciences, Taiwan.

[1] R. H. Dicke, Phys. Rev. **93**, 99 (1954).
[2] D. Polder, M. F. H. Schuurmans, and Q. H. F. Vrehen, Phys. Rev. A **19**, 1192 (1979).
[3] M. Gross and S. Haroche, Phys. Rep. **93**, 301 (1982).
[4] N. Skribanowitz, I. P. Herman, J. C. MacGillivray, and M. S. Feld, Phys. Rev. Lett. **30**, 309 (1973).
[5] M. Gross, C. Fabre, P. Pillet, and S. Haroche, Phys. Rev. Lett. **36**, 1035 (1976).
[6] H. M. Gibbs, Q. H. F. Vrehen, and H. M. J. Hikspoors, Phys. Rev. Lett. **39**, 547 (1977).
[7] E. Paradis, B. Barrett, A. Kumarakrishnan, R. Zhang, and G. Raithel, Phys. Rev. A **77**, 043419 (2008).
[8] R. Florian, L. O. Schwan, and D. Schmid, Phys. Rev. A **29**, 2709 (1984).
[9] M. S. Malcuit, J. J. Maki, D. J. Simkin, and R. W. Boyd, Phys. Rev. Lett. **59**, 1189 (1987).
[10] M. Dreher, E. Takahashi, J. Meyer-ter Vehn, and K.-J. Witte, Phys. Rev. Lett. **93**, 095001 (2004).
[11] G. T. Noe II, J.-H. Kim, J. Lee, Y. Wang, A. K. Wójcik, S. A. McGill, D. H. Reitze, A. A. Belyanin, and J. Kono, Nat. Phys. **8**, 219 (2012).
[12] D. A. G. Deacon, L. R. Elias, J. M. J. Madey, G. J. Ramian, H. A. Schwettman, and T. I. Smith, Phys. Rev. Lett. **38**, 892 (1977).
[13] M. Nagasono, J. R. Harries, H. Iwayama, T. Togashi, K. Tono, M. Yabashi, Y. Senba, H. Ohashi, T. Ishikawa, and E. Shigemasa, Phys. Rev. Lett. **107**, 193603 (2011).
[14] L. Mercadier, A. Benediktovitch, C. Weninger, M. A. Blessenohl, S. Bernitt, H. Bekker, S. Dobrodey, A. Sanchez-Gonzalez, B. Erk, C. Bomme *et al.*, Phys. Rev. Lett. **123**, 023201 (2019).
[15] T. Watanabe, X. J. Wang, J. B. Murphy, J. Rose, Y. Shen, T. Tsang, L. Giannessi, P. Musumeci, and S. Reiche, Phys. Rev. Lett. **98**, 034802 (2007).
[16] N. Cui, M. Macovei, K. Z. Hatsagortsyan, and C. H. Keitel, Phys. Rev. Lett. **108**, 243401 (2012).
[17] N. Cui, C. H. Keitel, and M. Macovei, Opt. Lett. **38**, 570 (2013).
[18] N. Cui and M. A. Macovei, Phys. Rev. A **96**, 063814 (2017).
[19] C. H. Keitel, M. O. Scully, and G. Süssmann, Phys. Rev. A **45**, 3242 (1992).
[20] V. Kozlov, O. Kocharovskaya, Y. Rostovtsev, and M. Scully, Phys. Rev. A **60**, 1598 (1999).
[21] G. Pert, J. Opt. Soc. Am. B **11**, 1425 (1994).
[22] N. Rohringer, D. Ryan, R. A. London, M. Purvis, F. Albert, J. Dunn, J. D. Bozek, C. Bostedt, A. Graf, R. Hill *et al.*, Nature (London) **481**, 488 (2012).
[23] C. Weninger and N. Rohringer, Phys. Rev. A **90**, 063828 (2014).
[24] H. Yoneda, Y. Inubushi, K. Nagamine, Y. Michine, H. Ohashi, H. Yumoto, K. Yamauchi, H. Mimura, H. Kitamura, T. Katayama *et al.*, Nature (London) **524**, 446 (2015).
[25] M. Schuurmans and D. Polder, Phys. Lett. A **72**, 306 (1979).
[26] Y. V. Shvyd'ko, T. Hertrich, U. van Bürck, E. Gerdau, O. Leupold, J. Metge, H. D. Rüter, S. Schwendy, G. V. Smirnov, W. Potzel *et al.*, Phys. Rev. Lett. **77**, 3232 (1996).
[27] R. Röhlsberger, K. Schlage, B. Sahoo, S. Couet, and R. Rüffer, Science **328**, 1248 (2010).
[28] W.-T. Liao, A. Pálffy, and C. H. Keitel, Phys. Lett. B **705**, 134 (2011).

[29] R. Röhlsberger, H. C. Wille, K. Schlage, and B. Sahoo, Nature (London) **482**, 199 (2012).
[30] W.-T. Liao, A. Pálffy, and C. H. Keitel, Phys. Rev. Lett. **109**, 197403 (2012).
[31] B. W. Adams, C. Buth, S. M. Cavaletto, J. Evers, Z. Harman, C. H. Keitel, A. Pálffy, A. Picón, R. Röhlsberger, Y. Rostovtsev *et al.*, J. Mod. Opt. **60**, 2 (2013).
[32] W.-T. Liao, A. Pálffy, and C. H. Keitel, Phys. Rev. C **87**, 054609 (2013).
[33] F. Vagizov, V. Antonov, Y. Radeonychev, R. Shakhmuratov, and O. Kocharovskaya, Nature (London) **508**, 80 (2014).
[34] W.-T. Liao and A. Pálffy, Phys. Rev. Lett. **112**, 057401 (2014).
[35] K. P. Heeg, J. Haber, D. Schumacher, L. Bocklage, H.-C. Wille, K. S. Schulze, R. Loetzsch, I. Uschmann, G. G. Paulus, R. Rüffer *et al.*, Phys. Rev. Lett. **114**, 203601 (2015).
[36] W.-T. Liao and S. Ahrens, Nature Photon. **9**, 169 (2015).
[37] K. P. Heeg, A. Kaldun, C. Strohm, P. Reiser, C. Ott, R. Subramanian, D. Lentrodt, J. Haber, H.-C. Wille, S. Goerttler *et al.*, Science **357**, 375 (2017).
[38] G.-Y. Wang and W.-T. Liao, Phys. Rev. Appl. **10**, 014003 (2018).
[39] R. Bonifacio, P. Schwendimann, and F. Haake, Phys. Rev. A **4**, 302 (1971).
[40] R. Bonifacio, P. Schwendimann, and F. Haake, Phys. Rev. A **4**, 854 (1971).
[41] J. Okada, K. Ikeda, and M. Matsuoka, Opt. Commun. **27**, 321 (1978).
[42] C. Brechignac and P. Cahuzac, J. Phys. B **14**, 221 (1981).
[43] J. Rai and C. M. Bowden, Phys. Rev. A **46**, 1522 (1992).
[44] F. Haake, H. King, G. Schröder, J. Haus, R. Glauber, and F. Hopf, Phys. Rev. Lett. **42**, 1740 (1979).
[45] F. Haake, H. King, G. Schröder, J. Haus, and R. Glauber, Phys. Rev. A **20**, 2047 (1979).
[46] F. T. Arecchi and E. Courtens, Phys. Rev. A **2**, 1730 (1970).
[47] R. Bonifacio, F. A. Hopf, P. Meystre, and M. O. Scully, Phys. Rev. A **12**, 2568 (1975).
[48] F. A. Hopf and P. Meystre, Phys. Rev. A **12**, 2534 (1975).
[49] Beam Parameters of European XFEL Radiation, https://www.xfel.eu/facility/instruments/scs/index_eng.html.
[50] R. Friedberg and S. R. Hartmann, Phys. Rev. A **13**, 495 (1976).
[51] J. Gunst, Y. A. Litvinov, C. H. Keitel, and A. Pálffy, Phys. Rev. Lett. **112**, 082501 (2014).
[52] N. ten Brinke, R. Schützhold, and D. Habs, Phys. Rev. A **87**, 053814 (2013).
[53] X. Zhang and A. A. Svidzinsky, Phys. Rev. A **88**, 033854 (2013).
[54] J. C. MacGillivray and M. S. Feld, Phys. Rev. A **14**, 1169 (1976).
[55] L. Yuan and A. A. Svidzinsky, Phys. Rev. A **85**, 033836 (2012).
[56] Y.-W. Lin, W.-T. Liao, T. Peters, H.-C. Chou, J.-S. Wang, H.-W. Cho, P.-C. Kuan, and I. A. Yu, Phys. Rev. Lett. **102**, 213601 (2009).
[57] S.-W. Su, Z.-K. Lu, S.-C. Gou, and W.-T. Liao, Sci. Rep. **6**, 35402 (2016).
[58] Q. H. F. Vrehen and J. J. der Weduwe, Phys. Rev. A **24**, 2857 (1981).
[59] N. E. Rehler and J. H. Eberly, Phys. Rev. A **3**, 1735 (1971).
[60] M. D. Crisp, Phys. Rev. A **1**, 1604 (1970).